Materials Science Forum Vols. 519-521 (2006) pp 1699-1706
online at http://www.scientific.net

Modeling of Porosity Formation in Aluminum Alloys

Kent D. Carlson[1,a], Zhiping Lin[1,b], Christoph Beckermann[1,c], George Mazurkevich[2,d] and Marc Schneider[2,e]

[1] Dept. Mechanical and Industrial Engineering, University of Iowa, Iowa City, Iowa 52242, USA

[2] MAGMA Giessereitechnologie GmbH, Kackertstrasse 11, D-52072 Aachen, Germany

[a]kdcarls@engineering.uiowa.edu, [b]zhipinglin@gmail.com, [c]becker@engineering.uiowa.edu
[d]gm@magmasoft.de, [e]M.Schneider@magmasoft.de

Keywords: porosity, aluminum alloys, hydrogen diffusion.

Abstract. A new approach based on microsegregation of gas dissolved in the melt is used to model pore formation during the solidification of aluminum alloys. The model predicts the amount and size of the porosity in a solidified casting. Computation of the micro-/macro-scale gas species transport in the melt is coupled with the simulation of the feeding flow and calculation of the pressure field. The rate of pore growth is calculated based on the local level of gas supersaturation in the melt. The effect of the microstructure on pore formation is also taken into account. Parametric studies for one-dimensional solidification under an imposed temperature gradient and cooling rate illustrate that the model captures important phenomena observed in porosity formation in aluminum alloys. Comparisons between predicted porosity percentages and previous experimental measurements show good correspondence.

Introduction

Porosity-related defects are a major cause of casting rejection and re-work in the casting industry. Porosity formation has been investigated by many researchers, dating back to the early 1-D microporosity modeling work of Piwonka and Flemings [1], and the seminal 2-D work of Kubo and Pehlke [2]. An extensive review of the research progress in microporosity modeling, from these early studies up to work done in 2000, is provided by Lee et al. [3]. Recent examples of porosity models for aluminum alloy castings, including the effect of dissolved hydrogen, can be found in Sabau and Viswanathan [4] and Pequet et al. [5]. All of these models assume the local diffusion of hydrogen in the melt to be infinitely fast. In a series of experimental and theoretical studies, Lee and coworkers [6-10] have shown that diffusion of hydrogen through the supersaturated liquid (inside the mushy zone) to the pore can be a rate-controlling factor in pore growth for aluminum alloys. Lee and Hunt [6,7] experimentally observed porosity formation in aluminum alloys using an X-ray temperature gradient stage. They found the pressure drop caused by shrinkage to be negligibly small. They developed a model of hydrogen diffusion-controlled growth by considering a single pore inside the mushy zone. The model does not compute the pressure field in the mushy zone; rather, the pressure is an input variable. Atwood et al. [8,9] applied this model to an Al7Si alloy, and Hamilton et al. [10] incorporated it into a heat flow model for complex-shaped castings, still neglecting pressure variations.

The present study of porosity formation in aluminum alloys focuses on incorporating into the porosity model of Carlson et al. [11] a model for local, finite-rate gas species diffusion through the liquid metal to the pores. As in Ref. [11], the pressure field and feeding flows in the liquid metal as well as in the mushy zone are determined using a single-domain approach. The model is tested for one-dimensional, directional solidification of the (un-modified) alloy A356 with a constant temperature gradient and cooling rate. The results are compared to measurements available in the literature. The importance of accounting for finite-rate diffusion of hydrogen to the pores is demonstrated.

Model Description

The present multi-phase model assumes that each volume element in the casting is composed of some combination of solid metal (*s*), liquid metal (*l*) and porosity (*p*), such that the volume fractions satisfy $\varepsilon_s + \varepsilon_l + \varepsilon_p = 1$. Mixture properties are obtained as the sum of the property values for each phase multiplied by their respective volume fractions. For example, the mixture density is given by: $\rho = \varepsilon_s \rho_s + \varepsilon_l \rho_l + \varepsilon_p \rho_p$. For the purpose of the parametric studies presented below, the temperature field is prescribed. The solid fraction (ε_s) is assumed to be known from solidification path data as a function of temperature.

The mixture continuity equation is simplified by assuming that the solid metal and the porosity are stationary. The continuity equation is then given by [11]

$$\frac{\partial}{\partial t}\left(\varepsilon_s \rho_s + \varepsilon_l \rho_l + \varepsilon_p \rho_p\right) + \nabla \cdot \left(\rho_l \mathbf{v}\right) = 0 \tag{1}$$

or

$$\nabla \cdot \mathbf{v} = -\frac{1}{\rho_l}\left[\frac{\partial}{\partial t}\left[\varepsilon_s\left(\rho_s - \rho_l\right) + \rho_l - \varepsilon_p\left(\rho_l - \rho_p\right)\right] + \mathbf{v} \cdot \nabla \rho_l\right] = CRHS\,, \tag{2}$$

where $\mathbf{v}$ denotes the superficial liquid velocity, $\mathbf{v} = \varepsilon_l \mathbf{v}_l$. Eq. 2 shows that the divergence of the velocity field is a function of the solidification contraction, liquid density change, porosity evolution, and gradients in the liquid density (although this last contribution is small).

The liquid momentum equation is given by [11]

$$\nabla^2 \mathbf{v} = \frac{\varepsilon_l}{K}\mathbf{v} + \frac{\varepsilon_l}{\mu_l}\nabla P - \frac{\varepsilon_l}{\mu_l}\rho_{ref}\mathbf{g}\,, \tag{3}$$

where P is the melt pressure, $\mathbf{g}$ is the gravity vector, ρ_{ref} is a reference liquid density, taken as the melt density at the liquidus temperature, and μ_l is the dynamic viscosity of the liquid, which is assumed constant and taken as the melt value at the liquidus temperature. Buoyancy-induced flow and inertial terms are neglected. The permeability, K, is given by $K = K_0\, \varepsilon_l^3/(1-\varepsilon_l)^2$, where $K_0 = \lambda_2^2/180$, in which λ_2 is the secondary dendrite arm spacing (SDAS). The SDAS is determined from $\lambda_2 = \left[\lambda_{2,0}^3 + M\left(t - t_L\right)\right]^{1/3}$, where $\lambda_{2,0}$ is an initial spacing (estimated as 20 μm in the present study), M is a coarsening constant (estimated as $M = 2600$ μm^3/s from experimental Al-7Si data [12]), and $\left(t - t_L\right)$ is the time (in seconds) elapsed since solidification began. Notice that Eq. 3 reduces to Stokes' equation in the single-phase liquid region, where K becomes very large. In the mushy zone, the left-hand side of Eq. 3 becomes very small relative to the permeability term, and the equation then reduces to Darcy's law.

By manipulating and combining Eq. 2 and Eq. 3, it is possible [11] to derive the following equation for the melt pressure, P:

$$\nabla \cdot \left(\frac{K}{\mu_l}\nabla P\right) = -\left(CRHS\right) + \nabla \cdot \left(\frac{K}{\mu_l}\rho_{ref}\mathbf{g}\right) + \nabla \cdot \left(\frac{K}{\varepsilon_l}\nabla^2 \mathbf{v}\right), \tag{4}$$

where $CRHS$ is the right-hand side of Eq. 2.

The average concentration of hydrogen dissolved in the melt, C_l (in wt fraction), is obtained from the mixture species conservation equation [11]

$$\frac{\partial}{\partial t}\left(\varepsilon_s \rho_s C_s + \varepsilon_l \rho_l C_l + \varepsilon_p \rho_p C_p\right) + \nabla \cdot \left(\rho_l C_l \mathbf{v}\right) = 0\,. \tag{5}$$

The concentration of hydrogen in the solid (assuming fast diffusion) is approximately $C_s = \kappa_{sl} C_l$, where κ_{sl} is the partition coefficient of hydrogen between the solid and liquid. Since the porosity is composed of hydrogen only, the hydrogen concentration in the pores is unity (i.e., $C_p = 1$).

An effective pore radius is calculated as in Pequet et al. [5] from

$$r_p = \mathrm{MAX}\left[r_0; \mathrm{MIN}\left(r_{sphere}; r_{dend}\right)\right], \tag{6}$$

where r_0 is a negligibly small initial pore radius (taken as 1 μm), $r_{sphere} = \left[3\varepsilon_p/(4\pi n)\right]^{1/3}$, in which n is the pore number density, and $r_{dend} = \lambda_2(1-\varepsilon_s)/(2\varepsilon_s)$. In the equation for r_{dend}, ε_s is held constant once the eutectic starts to form; also, r_{dend} is held constant once $r_p = r_{dend}$. In the latter case, the pores continue to grow between the dendrite arms by assuming an ellipsoidal shape; once the length of the (ellipsoidal) pores exceeds the distance between the pores ($\approx n^{-1/3}$), the pores are assumed to merge (creating so-called "connected" porosity).

The gas microsegregation equation is derived by combining the gas species balance at the interface between the pore and liquid phases with the pore phase gas species conservation equation - the details of the derivation will be presented elsewhere. With $C_p = 1$, the result can be written as:

$$\frac{\partial}{\partial t}\left(\varepsilon_p \rho_p\right) = \frac{S_{lp}\rho_l D_l}{l_{lp}} \frac{\left(C_l - C_{lp}\right)}{1 - C_{lp}} = \gamma_{lp}\Omega_l, \tag{7}$$

where C_{lp} is the equilibrium concentration of hydrogen in the liquid at the pore/liquid interface (in wt fraction), S_{lp} is the interfacial area concentration of the pores (pore surface area per unit volume), D_l is the mass diffusivity of hydrogen in the melt, and l_{lp} is a liquid diffusion length at the pore/liquid interface. The second equality in Eq. 7 defines a pore growth factor $\gamma_{lp} = S_{lp}\rho_l D_l / l_{lp}$ and a normalized liquid supersaturation $\Omega_l = \left(C_l - C_{lp}\right)/\left(1 - C_{lp}\right)$. The interfacial area concentration is approximated as $S_{lp} = 4\pi n r_p^2 \phi$, where ϕ is an impingement factor taken as $1 - \varepsilon_s$. The diffusion length is calculated from $l_{lp} = r_p$, which is based on the well-known analytical result for the species boundary layer thickness around a sphere. Figure 1 illustrates the concept of the species diffusion length. For a finite supersaturation in the melt, when the average gas species concentration C_l is larger than the equilibrium concentration at the pore/liquid interface C_{lp}, hydrogen diffuses towards the pore and the pore grows (i.e., ε_p increases). For large γ_{lp}, which occurs for a large interfacial area (e.g., with a high pore density, n) and/or a small diffusion length, the melt becomes well-mixed (C_l tends to C_{lp}), since the pore growth rate $\partial\left(\varepsilon_p \rho_p\right)/\partial t$ must be finite. Note from Eq. 7 that the pore volume fraction, ε_p, also changes in response to changes in the pore density, ρ_p. The pore density is calculated from the ideal gas law, $\rho_p = P_p/(RT)$, where P_p is the pore pressure, R is the gas constant for hydrogen, and T is the absolute temperature. In the present model, Eq. 7 is actually solved for the equilibrium concentration at the liquid/pore interface, C_{lp}. As in Ref. [11], the pore volume fraction ε_p is then determined from the continuity equation, Eq. 1. Hence, the effects of feeding flow, solidification shrinkage, and other density changes on ε_p are still taken into account.

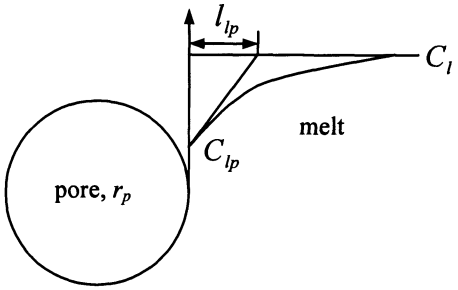

Figure 1. Hydrogen diffusion boundary layer around a growing pore.

The pore pressure is calculated from Sievert's law

$$\frac{P_p}{P_{atm}} = \left[\frac{C_{lp}}{(K_e/f)}\right]^2. \tag{8}$$

When no pores are present, C_l is used in place of C_{lp}. In Eq. 8, K_e (in wt fraction) and f are the equilibrium and activity coefficients of the hydrogen gas species, respectively. The equilibrium coefficient is a function of temperature, given by $\log_{10} K_e = -a/T - b$, where a and b are constants. The activity coefficient is calculated as a function of the silicon and copper concentrations in the melt by $\log_{10} f = e_H^{Si} C_l^{Si} + r_H^{Si} \left(C_l^{Si}\right)^2 + e_H^{Cu} C_l^{Cu} + r_H^{Cu} \left(C_l^{Cu}\right)^2$, where C_l^{Si} and C_l^{Cu} are the concentrations (in wt pct) of silicon and copper in the melt, and e_H and r_H are interaction coefficients given in Ref. [13]. It should be noted that Ref. [13] gives interaction coefficients for several other elements (Mg, Fe, Zn, etc.), but states that the coefficients for these elements are "of rather uncertain accuracy." Thus, they were not included in the present model. For the A356 alloy, the effect of Cu and other elements on the solubility is small compared to the effect of Si. Until the eutectic forms, the melt concentrations are approximately given by the Scheil equation as $C_l^{Si} = C_0^{Si}\left(1-\varepsilon_s\right)^{\kappa^{Si}-1}$ and $C_l^{Cu} = C_0^{Cu}\left(1-\varepsilon_s\right)^{\kappa^{Cu}-1}$, where C_0^{Si} and C_0^{Cu} are the initial concentrations of these elements, and κ^{Si} and κ^{Cu} are the partition coefficients for silicon and copper in the aluminum alloy. During and after eutectic formation, the activity coefficient is held constant at the eutectic value.

The capillary pressure is modeled as

$$P_\sigma = \frac{2\sigma}{\mathrm{MAX}\left(r_p; r_{nuc}\right)}, \tag{9}$$

where σ is the surface tension. The effective pore radius at nucleation, r_{nuc}, may be calculated from $r_{nuc} = r_0/\Phi$, where Φ is a heterogeneous nucleation parameter (less than unity). However, neither the initial pore radius nor the heterogeneous nucleation parameter are known to any degree of accuracy. Furthermore, pores may not actually nucleate in the melt, but can evolve from small gas pockets inside entrained oxide films. Therefore, r_{nuc} is simply used in the present study as a parameter to control the *maximum* capillary pressure at which the pores nucleate or start to grow. Once $r_p > r_{nuc}$, Eq. 9 gives the capillary pressure corresponding to a pore of radius r_p.

Porosity is assumed to nucleate if $P \le P_p - P_\sigma$. When porosity forms, the melt pressure at that location is forced to $P = P_p - P_\sigma$ [11].

Results

Numerical simulations were conducted for directional solidification of the aluminum alloy A356. Due to space limitations, it is not possible to list all of the thermophysical properties used in the simulations. Suffice it to say that they were collected from Refs. [5,9,12-16]. The system domain is one-dimensional (in x) with a zero flow boundary condition at the left ($x = 0$) side and atmospheric pressure applied at the right (inflow) boundary. A linear temperature profile is translated across the domain with a speed given by $\dot{T}/G$, where $\dot{T}$ is the cooling rate. In all but the last result shown, the temperature gradient, G, is held constant at $G = 500$ °C/m.

Figure 2 shows profiles of some of the calculated dependent variables for an initial hydrogen level in the melt of $C_0 = 0.13$ $cc_{STP}H_2/100g$ Al and a cooling rate of 0.5°C/s. The pore density in this simulation is 10^9 m^{-3}, and the maximum capillary pressure, $P_{\sigma,nuc} = 2\sigma/r_{nuc}$, is 1.6 bar, which corresponds to $r_{nuc} \approx 10$ μm. The temperature increases linearly in the positive x-direction. Results are shown at a time in the simulation when there is a fully solidified layer next to $x = 0$. Figure 2a indicates that the porosity starts to form at the beginning of the eutectic reaction (when the liquid fraction, ε_l, is about 35%). The pore fraction continues to increase until the melt is completely solidified. The melt pressure drop is very small before the eutectic reaction; subsequently, the melt pressure P decreases more significantly, due to the permeability decreasing strongly as the liquid fraction approaches zero. The pore pressure, P_p $(= P + P_\sigma)$, reflects this decrease during pore growth. The P_p profile before pore formation illustrates the increase in the equilibrium gas pressure

with decreasing temperature according to Sievert's law. Note that the capillary pressure, P_σ, rapidly reduces from the initial value of $P_{\sigma,nuc} = 1.6$ bar to about 0.9 bar due to the increase in the pore radius, r_p, during the initial pore growth stage; subsequently, P_σ remains constant at 0.9 bar, because r_p is limited by the dendritic network (r_{dend}). Figure 2b illustrates the development of the hydrogen supersaturation in the melt. Before porosity formation, the average hydrogen concentration in the melt, C_l, increases with decreasing temperature because of rejection (partitioning) of hydrogen from the growing solid; the equilibrium concentration, C_{lp}, from Sievert's law decreases primarily because of the decreasing temperature. At the point where porosity starts to form, $C_l = C_{lp}$. Then, the concentration C_l rapidly increases due to the high rate of solidification during eutectic formation, while C_{lp} continues to decrease. The difference $C_l - C_{lp}$ in Fig. 2b reflects the significant level of hydrogen supersaturation in the melt during pore growth. Also note that the growth factor γ_{lp} varies considerably during pore formation.

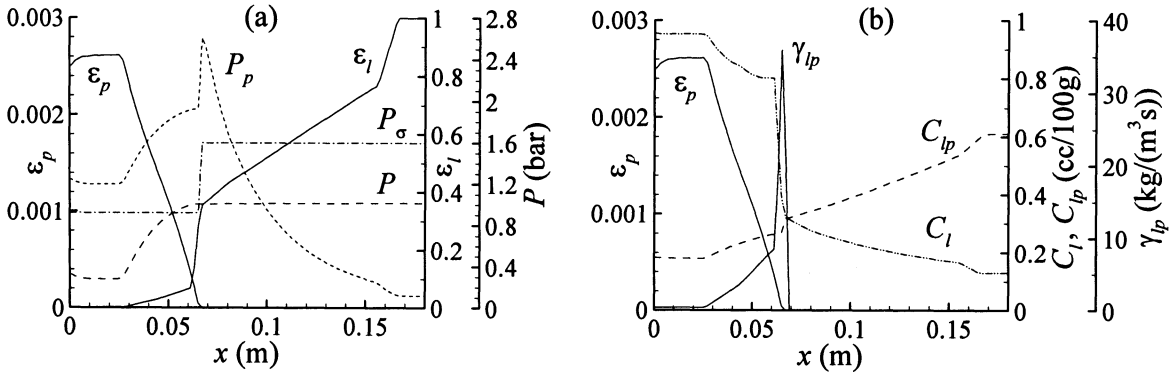

Figure 2. Profiles of computed variables during directional solidification of A356.

Before exploring the effect of finite-rate diffusion of hydrogen in the liquid in more detail, it is important to better understand the role of the maximum capillary pressure at the beginning of pore growth, $P_{\sigma,nuc}$, on porosity formation. Thus, a number of simulations were performed where the growth factor, γ_{lp}, was set to a very large value, thereby modeling complete (infinitely fast) local diffusion of hydrogen in the melt. The results, shown in Fig. 3, correspond to $\dot{T} = 1$ °C/s and $n = 10^{11}$ pores/m^3 (note that for $\gamma_{lp} \to \infty$, n has almost no effect on the results). In Fig. 3a, the calculated final pore volume percentage (at steady state) is plotted as a function of the initial hydrogen content, C_0, for $P_{\sigma,nuc} = 0$, 1.6, and 16 bar. For $P_{\sigma,nuc} = 0$, ε_p increases almost linearly with increasing C_0. At a given gas level, the porosity levels are significantly lower for the two finite $P_{\sigma,nuc}$. Interestingly, the predicted variations of ε_p with C_0 are quite similar for $P_{\sigma,nuc} = 1.6$ and 16 bar, except that a more pronounced "threshold" hydrogen level of $C_0 \approx 0.06$ $cc_{STP}H_2/100g$ Al, below which $\varepsilon_p \approx 0$, can be observed for $P_{\sigma,nuc} = 16$ bar. This indicates that for reasonably large $P_{\sigma,nuc}$ (and C_0 well above the threshold hydrogen level), the capillarity effect ceases to have an important influence on the final porosity levels. Note that $P_{\sigma,nuc} = 1.6$ bar is a physically reasonable value, whereas 16 bar is much too high. Finally, note the small but finite values of porosity seen in Fig. 3a for low values of C_0. This porosity is shrinkage porosity that remains when the hydrogen level approaches zero. As seen in Fig. 3b, it does not form until solidification is almost complete (solid fraction above 95%). It could be argued that the remaining shrinkage porosity should be larger due to the presence of encapsulated liquid pockets at high fractions solid. However, Fang and Granger [17] measured porosity values less than 0.05% for low hydrogen levels, indicating that the encapsulated liquid pocket effect cannot be important. Even though the present permeability model does not completely cut off the feeding flow (via zero permeability) until the melt is completely solidified, the pressure reaches low enough values for some shrinkage porosity to form.

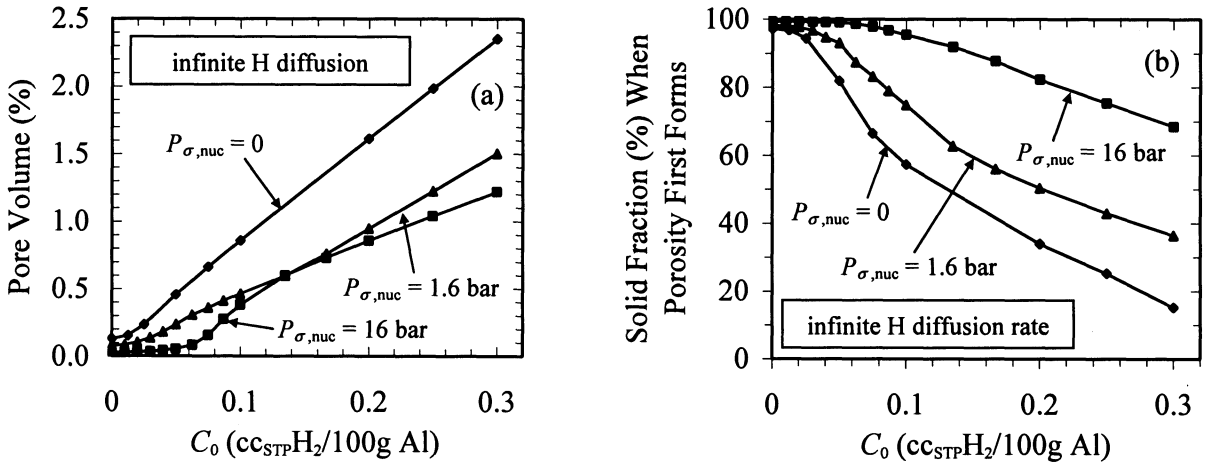

Figure 3. Predicted steady-state results for infinitely fast local diffusion of hydrogen in the melt ($\gamma_{lp} \to \infty$): variation of pore volume (a) and solid fraction at pore formation (b) with C_0.

The predicted values of the solid fraction at which porosity first forms are plotted as a function of C_0 in Fig. 3b, for $P_{\sigma,nuc} = 0$, 1.6, and 16 bar. For $C_0 \to 0$, porosity starts to form at solid fractions close to unity, indicating as before that for $\dot{T} = 1$ °C/s, the shrinkage contribution to the porosity is negligibly small. With increasing initial hydrogen content, the solid fraction at which porosity first forms decreases strongly. In fact, for relatively large initial hydrogen contents (with the more reasonable value of $P_{\sigma,nuc} = 1.6$ bar), porosity can evolve at low solid fractions (e.g., 40%), well before any eutectic starts to form. At a given initial hydrogen content, the solid fraction at which porosity first forms increases strongly with increasing $P_{\sigma,nuc}$. In other words, the higher the maximum capillary pressure, the later during solidification that porosity starts to form.

The effect of finite-rate diffusion of hydrogen in the liquid on pore formation, as modeled by Eq. 7, is explored in Fig. 4. The initial hydrogen content is fixed at $C_0 = 0.13$ cc$_{STP}$H$_2$/100g Al, and $P_{\sigma,nuc}$ at 1.6 bar. Figure 4a shows predicted pore volume percentages as a function of cooling rate, with G held constant at 500°C/m, for three sets of simulations: (1) $\gamma_{lp} \to \infty$ (infinitely fast diffusion) and $n = 10^{11}$ m^{-3}; (2) γ_{lp} finite and $n = 10^{11}$ m^{-3}; and (3) γ_{lp} finite and $n = 10^{9}$ m^{-3}. Focusing first on Case 1 (infinitely fast local diffusion of hydrogen in the liquid), it can be seen that the pore volume is relatively independent of the cooling rate for $\dot{T}$ below about 5°C/s. This indicates that at low cooling rates, feeding flow effects are not important. For larger cooling rates, however, the pore volume percentage increases strongly with increasing $\dot{T}$. This can be explained by the increasing liquid pressure drop in the mush, since a higher cooling rate causes (i) higher feeding velocities and (ii) smaller secondary dendrite arm spacings which, in turn, reduce the permeability. The liquid pressure drop is the basis for the well-known Niyama criterion, which is a thermal parameter given by the ratio $G/\sqrt{\dot{T}}$. Generally, porosity increases with a decreasing Niyama criterion value (e.g., with an increasing cooling rate) [20]. Based on its derivation, the Niyama criterion applies to shrinkage or feeding-flow-related porosity only, and not to gas porosity (note that the dissolved gas content is not even a parameter in the Niyama criterion). In solidification of the A356 alloy with a relatively low hydrogen level, shrinkage or feeding flow effects come into play only at high cooling rates (i.e., $\dot{T} > 5-10$ °C/s). At low cooling rates (i.e., $\dot{T} < 5$ °C/s), the liquid pressure drop is relatively small due to the large fraction of eutectic (see Fig. 2), and shrinkage porosity is negligibly small. At high cooling rates (and relatively low hydrogen levels), however, the pressure drop is significantly larger and shrinkage does become important.

For Cases 2 and 3, which have a finite pore growth factor γ_{lp}, Fig. 4a shows that for a given cooling rate, the predicted pore volume percentages are significantly lower than for $\gamma_{lp} \to \infty$ (Case 1), as expected. In particular, for Case 3, the pore volume percentages decrease steeply with increasing cooling rate up to about 1°C/s. This steep decrease would not be possible without

accounting for the reduction in the pore growth rate due to finite-rate diffusion of hydrogen in the melt. The finite-rate diffusion effect becomes stronger with increasing cooling rate because less time is available for diffusion. Only as the cooling rate tends to zero (very long solidification times) do the predictions for the three cases approach each other. For cooling rates above 5–10 °C/s, Cases 2 and 3 show the same kind of increase in ε_p with $\dot{T}$ as Case 1, as explained above by the Niyama criterion. Since the pore growth factor is smaller for a lower pore number density (i.e., $\gamma_{lp} \sim n$), the predicted pore volume percentages for $n = 10^9$ m^{-3} (Case 3) are smaller than for 10^{11} m^{-3} (Case 2). They remain lower even for high cooling rates, when shrinkage becomes important, because the finite-rate diffusion effect also becomes stronger with increasing $\dot{T}$.

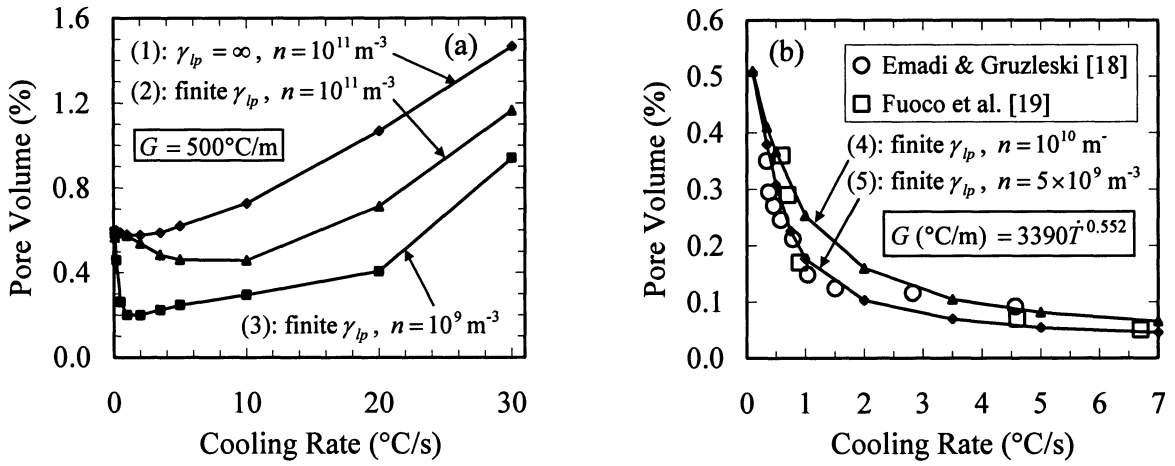

Figure 4. Variation of pore volume percentage with cooling rate for C_0 = 0.13 $cc_{STP}H_2$/100g Al, showing (a) results for a constant temperature gradient, and (b) a separate study that considered the variation of temperature gradient G with cooling rate, compared with experimental data [18,19].

Figure 4b shows previously measured pore volume percentages as a function of cooling rate [18, 19]. The experiments in Refs. [18,19] were performed using setups where solidification proceeds upward in an essentially one-dimensional manner, with strong chilling at the bottom and insulated lateral walls. In order to determine approximate temperature gradients corresponding to the cooling rates reported, the experiments were simulated using commercial casting simulation software. The cooling rates reported in Ref. [18] are average values over the freezing range. Heat transfer coefficients were adjusted until the simulated cooling rates compared favorably to those measured in Refs. [18,19]. The temperature gradient corresponding to a given cooling rate was then estimated from simulation data, again averaged over the freezing range. Then, a curve fit was used to relate the predicted temperature gradient to the cooling rate, leading to the following expression: $G = 3390\dot{T}^{0.552}$, where G is in °C/m, and $\dot{T}$ is in °C/s. Even though all results in Refs. [18,19] are reported as a function of cooling rate only (which decreases with distance from the bottom chill), the fit shows that the temperature gradient varies significantly too. Using the above expression relating G and $\dot{T}$, two more sets of simulations were performed: (4) γ_{lp} finite and $n = 10^{10}$ m^{-3}; and (5) γ_{lp} finite and $n = 5\times10^9$ m^{-3}. These pore number densities approximately correspond to the image analysis data in Ref. [18]. The results of these simulations are also given in Fig. 4b, and they are seen to agree well with the measured pore volume percentages. The predictions for Cases 4 and 5 nicely envelop the experimental data. Most importantly, it would not have been possible to predict the measured steep decrease in ε_p for cooling rates up to about 1°C/s without a model that accounts for local finite-rate diffusion of hydrogen in the liquid. The continued, but more gradual, decrease in the pore volume percentage for higher cooling rates can be attributed to the temperature gradient increasing with $\dot{T}$ (otherwise ε_p would increase as shown in Fig. 4a). A higher

temperature gradient causes the liquid pressure drop across the (more narrow) mush to be smaller and, hence, reduces the shrinkage porosity at higher cooling rates (see Fig. 4a). This effect can again be inferred from the Niyama criterion ($G/\sqrt{\dot{T}}$), since porosity generally decreases with an increasing Niyama criterion value (note that $G/\sqrt{\dot{T}} = 3390\dot{T}^{0.052}$, which is an increasing function of $\dot{T}$).

Conclusions

A gas microsegregation model has been developed for porosity formation in aluminum alloys. By incorporating the effect of local, finite-rate diffusion of dissolved hydrogen in the liquid into an existing porosity model [11], the effects of feeding flow and melt pressure are taken into account as well. The comparisons with previous experimental measurements show that pore growth can indeed be limited by finite-rate diffusion of hydrogen, but that shrinkage driven porosity can still be important for high cooling rates and low temperature gradients. The model is general in that it can be immediately applied to fully three-dimensional casting situations, as demonstrated in Ref. [11] without gas microsegregation.

References

[1] T.S. Piwonka and M.C. Flemings: Trans. AIME Vol. 236 (1966), p. 1157.

[2] K. Kubo and R.D. Pehlke: Metall. Trans. B Vol. 16B (1985), p. 359.

[3] P.D. Lee, A. Chirazi, and D. See: J. Light Metals Vol. 1 (2001), p. 15.

[4] A.S. Sabau and S. Viswanathan: Metall. Mater. Trans. B Vol. 33B (2002), p. 243.

[5] Ch. Pequet., M. Gremaud, and M. Rappaz: Metall. Mater. Trans. A Vol. 33A (2002), p. 2095.

[6] P.D. Lee and J.D. Hunt: Modeling of Casting, Welding and Advanced Solidification Processes VII, ed. M. Cross and J. Campbell (TMS, Warrendale, Pennsylvania, USA, 1995), p. 585.

[7] P.D. Lee and J.D. Hunt: Acta Mater. Vol. 45 (1997), p. 4155.

[8] R.C. Atwood, S.Sridhar, W. Zhang and P.D. Lee: Acta Mater. Vol. 48 (2000), p. 405.

[9] R.C. Atwood and P.D. Lee: Metall. Mater. Trans. B Vol. 33B (2002), p. 209.

[10] R.W. Hamilton, D. See, S. Butler, and P.D. Lee: Mat. Sci. Eng. Vol. A343 (2003), p. 290.

[11] K.D. Carlson, Z. Lin, R.A. Hardin, C. Beckermann, G. Mazurkevich, and M.C. Schneider: Modeling of Casting, Welding and Advanced Solidification Processes X, ed. D.M. Stefanescu et al. (TMS, Warrendale, Pennsylvania, USA, 2003), p. 295.

[12] S. Shivkumar, D. Apelian, J. Zou: AFS Trans. Vol. 98 (1990), p. 897.

[13] G.K. Sigworth and T.A. Engh: Metall. Trans. B Vol. 13B (1982), p. 447.

[14] *MAGMASOFT*, MAGMA GmbH, Kackerstrasse 11, 52072 Aachen, Germany.

[15] D. Emadi, J.E. Gruzleski and J.M. Toguri: Metall. Trans. B Vol. 24B (1993), p. 1055.

[16] G.K. Sigworth and C. Wang: AFS Trans. Vol. 100 (1992), p. 989.

[17] Q.T. Fang and D.A. Granger: AFS Trans. Vol. 97 (1989), p. 989.

[18] D. Emadi and J.E. Gruzleski: AFS Trans. Vol. 102 (1994), p. 307.

[19] R. Fuoco, H. Goldenstein and J.E. Gruzleski: AFS Trans. Vol. 102 (1994), p. 297.

[20] K.D. Carlson, S. Ou, R.A. Hardin, and C. Beckermann: Metall. Mater. Trans. B Vol. 33B (2002), p. 731.